Aerodynamic Effects of Gurney Flaps
on the Rotor Blades of a Research Wind Turbine

Joerg Alber[1], Rodrigo Soto-Valle[1], Marinos Manolesos[2], Sirko Bartholomay[1], Christian Navid Nayeri[1], Marvin Schoenlau[1], Christian Menzel[1], Christian Oliver Paschereit[1], Joachim Twele[3], Jens Fortmann[3]

[1]Technische Universität Berlin, Hermann-Föttinger Institut, Müller-Breslau-Str. 8, 10623 Berlin, Germany
[2] College of Engineering, Swansea University, Bay Campus, Fabian Way, Swansea, SA1 8EN, UK
[3] Hochschule für Technik und Wirtschaft Berlin, Wilhelminenhofstraße 75A, 12459 Berlin, Germany

Correspondence to: Joerg Alber (joerg.alber@htw-berlin.de)

Abstract.

This paper investigates the aerodynamic impact of Gurney flaps on the rotor blades of a research wind turbine of the Hermann-Föttinger Institute at the Technische Universität Berlin. The rotor radius is 1.5 meters and the blade configurations consist of the clean and the tripped baseline cases emulating the effects of leading edge roughness. The wind tunnel experiments include three operation points based on tip speed ratios of 3.0, 4.3 and 5.6, reaching Reynold numbers of approximately 250,000. The measurements are taken by means of three different methods; Ultrasonic Anemometry in the wake, surface pressure taps in the mid-span blade region and strain gauges at the blade root. The retrofit application consists of two Gurney flap heights of 0.5 % and 1.0 % in relation to the chord length, which are implemented perpendicular to the pressure side at the trailing edge. As a result, the Gurney flap configurations evoke performance improvements in terms of the axial wake velocities, the angles-of-attack and the lift coefficients. Furthermore, the aerodynamic impact appears to be more pronounced in the tripped case compared to the clean case. The enhancement of the root bending moments imply an increase of both the rotor thrust and torque. Gurney flaps are considered a worthwhile passive flow-control device in order to alleviate the adverse effects of both early separation in the inner blade region and leading edge erosion of horizontal axis wind turbines.

1 Introduction

The energy yield of modern Horizontal Axis Wind Turbines (HAWTs) is supposed to be optimal and the maintenance costs minimal while completing a lifetime of around 20 years. However, the performance of rotor blades faces serious challenges, two of which are early separation and roughness effects. Early separation is a problem especially in the inner blade region where the Angles-of-attack (AoA) are elevated due to structural constraints, such as limited chord-lengths and twist-angles (Figure 1 (a)). Over time, the resulting dynamic loads contribute to the material fatigue of the blade. At the same time, roughness effects are evoked by the longstanding surface erosion throughout the entire blade span, especially close to the

1

30   Leading Edge (LE), as shown in Figure 1 (b). Apart from the broad range of weather conditions, surface roughening is aggravated by rain, insects as well as sand or salt particles. Hence, the energy yield of HAWTs is often found lower than predicted or regressing over time (Wilox et al., 2017).

(a)   (b)

Figure 1. Rotor blades of utility scale wind turbines (a) Flow indicators to detect early separation in the root region, reproduced and modified from Pechlivanoglou et al. (2013). (b) Leading edge roughness, reproduced and modified from Pechlivanoglou et al. (2010).

35   This paper investigates an aerodynamic approach aiming at the alleviation of the mentioned challenges; the retrofit application of Gurney Flaps (GFs). This passive flow-control device consists of a wedge- or right angle profile that is attached perpendicular to the pressure side at the Trailing Edge (TE) of wings or blades. The GF-height in relation to the local chord-length is the main aerodynamic parameter, as shown in Figure 2 (a). It is usually in the range of 0.5 %c $< GF <$ 2.0 %c without taking the TE thickness into account.

(a)   (b)
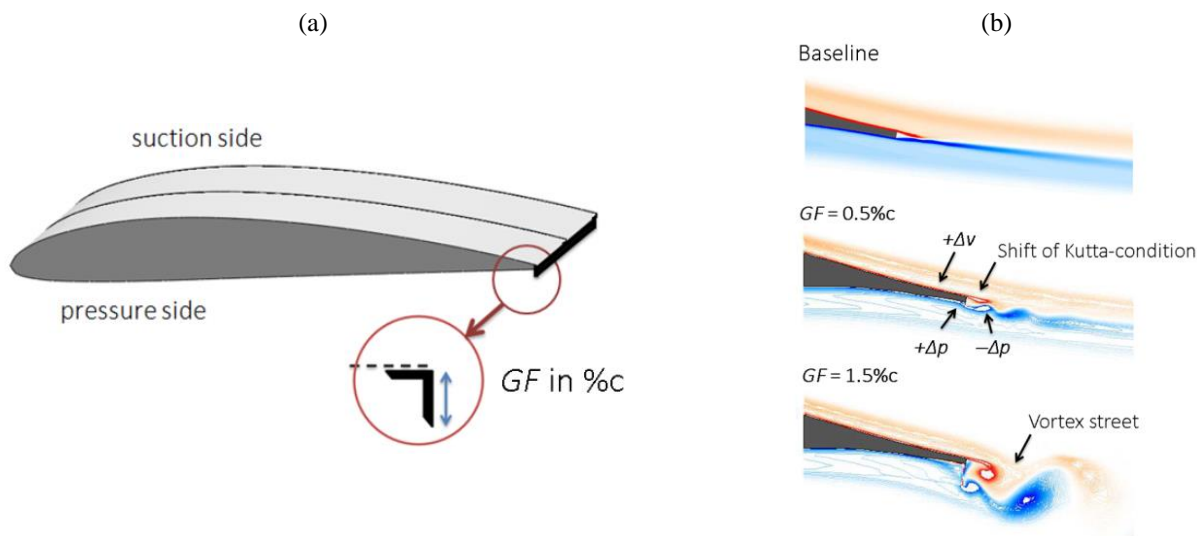
40   **Figure 2.** (a) Position of the Gurney Flap at the trailing edge of a generic Clark-Y airfoil section. (b) CFD-simulation of the HQ17 airfoil at $Re = $ 1M, reproduced and modified from Schatz et al. (2004).

2

The research on TE flaps of airplane-wings dates back to the early 20th century (Gruschwitz and Schrenk, 1933). The GF itself is named after the racecar driver Dan Gurney, who discovered the significant gain in downforce when applying the device on the rear spoilers of his vehicles. Following from that, GFs have been implemented on certain high lift-dependent transport airliners (Bechert et al., 2000) and helicopter stabilizers (Houghton, 2013). More recently, Vestas® has started offering GFs in combination with Vortex Generators (VGs) as an aerodynamic upgrade of HAWTs, predicting annual yield improvements of up to 2 %. The design of the DTU 10 MW Reference turbine includes smooth wedge-shaped GFs in the first half of the blade length, $0.05R < r < 0.4R$, and with GF-heights in the range of $3.5 \%c < GF < 1.3 \%c$ (Bak et al., 2013).

Figure 2 (b) illustrates the changes in the flow field of a generic airfoil section when implementing different GF-heights, as previously reported by Liebeck (1978). Key to the aerodynamic understanding is the development of one vortex upstream and two counter-rotating vortices downstream of the GF, as such entailing a low pressure region in the TE wake. As a result, the downwash angle of the flow becomes steeper, the requirements for pressure recovery on the suction side milder, the local boundary layer thinner and the suction peak higher. Additionally, the flow on the pressure side decelerates leading to a positive pressure built-up in the TE region. The resulting shift in the Kutta condition is evoking increased circulation and thus higher lift, one of the main Gurney flap characteristics. At the same time, the low pressure region aft the TE induces additional drag, especially if vortex shedding is initiated in the form of a Kármán vortex street. Hence, the lift increase is accompanied by a certain drag penalty that affects the Lift-to-Drag (L/D) ratio accordingly.

For that reason, various experimental and numerical research projects have aimed to limit the adverse drag increase while maintaining the beneficial lift enhancement of GFs. Giguère et al. (1995) and Kentfield (1996) conclude that the GF-height is supposed to be submerged into the local Boundary Layer (BL) in order to keep the drag on an acceptable level. Bechert et al. (2000) demonstrates that additional holes, slits and especially the pattern of dragonfly wings lead to reduced drag on the laminar airfoil HQ17 at Re = 1M. In addition, promising results are presented for very small GF-heights in the range of $0.2 \%c < GF < 0.5 \%c$, as such substantially lower than the BL thickness at the TE. Following from that, CFD-based wake simulations of Schatz et al. (2004) reveal that the induced drag depends on the GF-height, in fact in a disproportionate manner. As such, Figure 2 (b) illustrates that in the case of $GF = 1.5 \%c$ a vortex street is triggered while for $GF = 0.5 \%c$ the wake is shed in a relatively smoother manner. On a similar line, Alber et al. (2017) suggests the use of very small GF-heights of approximately half the local BL thickness in order to achieve the lift enhancement while maintaining, or even improving, the airfoil L/D-ratio.

The present investigation applies the aforementioned design principles on a research turbine using GF-heights of 0.5 %c and 1.0 %c. In addition, forced LE transition is evoked in order to emulate roughness effects, as discussed in Sect. 2.2.1. The impact of retrofit GFs is investigated based on the following experiments:

- 3D Ultrasonic Anemometry in the turbine wake to determine the local AoA.

- Pressure taps in the mid-span blade region to determine the local lift performance.

75 - Strain gauges at the blade root to determine the flapwise and the edgewise root bending moments.

In the remaining of the paper, the experimental set up is described in detail, followed by the presentation and discussion of the results. The main conclusions are drawn in the final section of this report.

2 Experimental set-up

2.1 Berlin Research Turbine

80 The Berlin Research Turbine (BeRT) is a test bench of the closed-loop wind tunnel at the Hermann-Föttinger Institut of the Technische Universität Berlin. It is a unique wind turbine demonstrator to explore specific fluid-dynamic phenomena based on a fully equipped rotating system (Vey et al., 2015). In recent years, the BeRT has facilitaded a multitude of experimental and numerical research projects, many of which are mentioned throughout this paper.
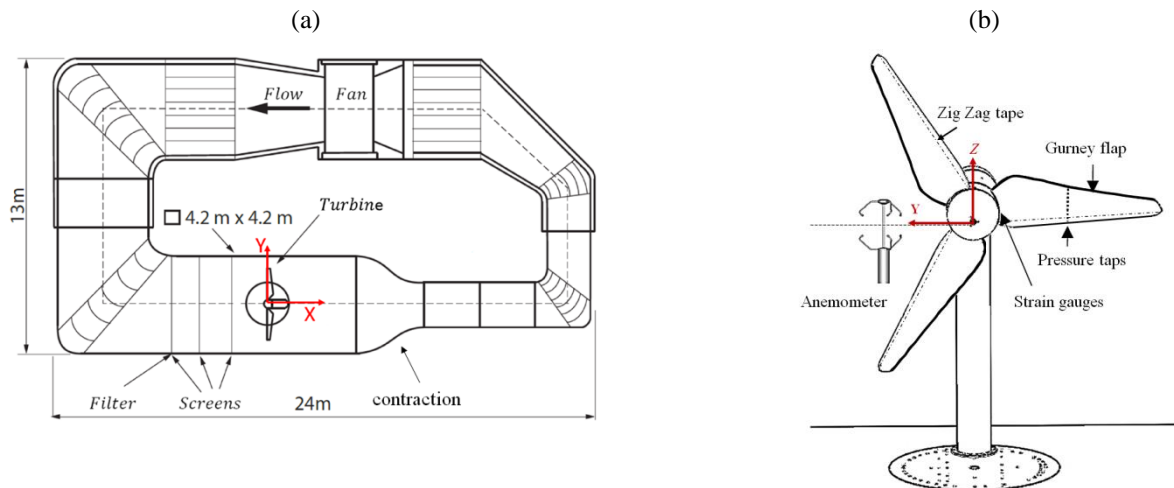
(a)   (b)

Figure 3. (a) Closed-loop wind tunnel in top-view. (b) BeRT set-up in front-view looking downstream.

85 In Figure 3 (a) the wind tunnel facility is depicted consisting of the high speed (2.0m x 1.4m) and the low speed (4.2m x 4.2m) test section. The BeRT is situated in the low speed test section downstream of the flow-conditioning screens and upstream of the wind tunnel contraction. The maximum inflow velocity is 10 ms^{-1}. The third screen upstream the rotor plane is equipped with an additional turbulence filter mat (Vildedon P15/150s) in order to reduce the turbulence intensity to 1.0 % $< Ti <$ 1.5 % (Bartholomay et al., 2017).

90

Figure 3 (b) displays the BeRT set-up and the measurement methods applied. The rotor radius is $R = 1.5$ m causing a relatively high blockage ratio of approximately 40 %. As follows, relative distances are expressed in relation to the rotor radius, R, and the zero position at the center of the rotor plane at $X = Y = Z = 0$. The blades are based on the low Reynolds profile Clark-Y with a maximum thickness of 11.9 %c. The blade geometry is optimized aerodynamically while both the chord-length and the twist-angles are decreasing in a linear way from root to tip alongside most of the blade length. The root section is contiguous to the round rotor hub and the tip section is pointy, as shown in Figure 4. The tip speed ratio at rated conditions is $TSR = 4.3$, developing a span-wise Re range from root to tip of $170k < Re < 300k$. The axial inflow velocity is captured by two parallel Prandtl tubes that are permanently installed at approximately one rotor radius upstream, close to each wind tunnel wall and slightly above hub-height. At rated conditions, the inflow velocity is 6.5 ms^{-1} at a rotational frequency of $f_{rot} = 3$ Hz (Table 1). The data acquisition (DAQ) system of the rotating sensors, such as pressure taps and strain gauges, is installed within the rotational spinner (Figure 6 (a)). The electrical power is transferred to the rotating system through a slip ring. Communication with the host PC is established via WIFI connection in order to set and modify the rotational speed. The DAQ system captures all channels simultaneously at 10 kHz and streams the data to a host PC via network connection.

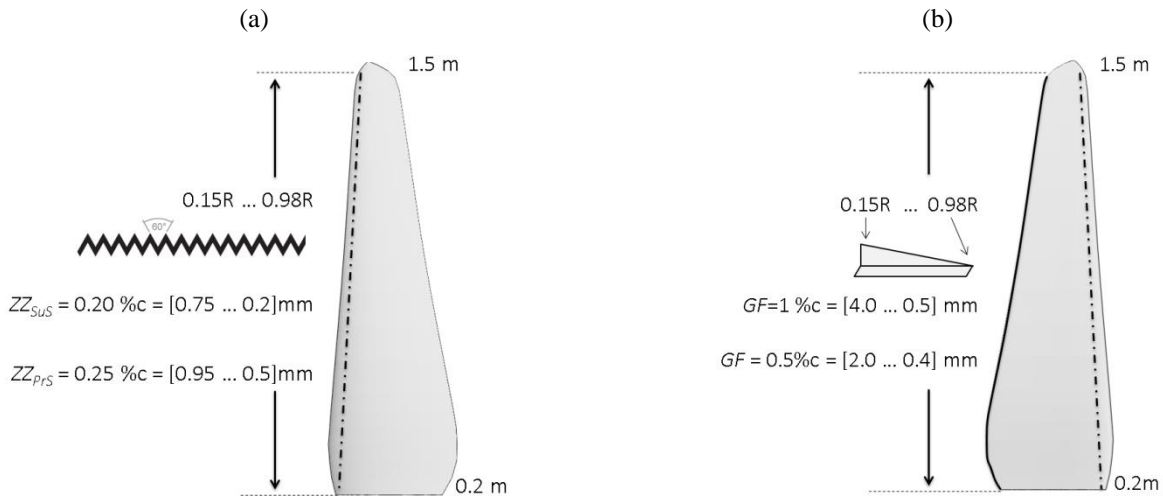## 2.2. Blade configurations and operation points

2.2.1 Forced transition

The principal baseline configuration of the BeRT includes Zig Zag (ZZ) turbulator tape or the tripped case. In addition, the clean blade configuration is investigated for comparative purposes. ZZ tape is applied in order to initiate the laminar-to-turbulent transition of the Boundary Layer (BL) at a fixed location. In practical terms, it is used to emulate LE roughness-effects on airfoil sections (Rooij and Timmer, 2003) and rotor blades (Zhang et al., 2017). Its height is slightly smaller than the local BL thickness in order to trigger the complete BL transition while avoiding the disproportionate increase of drag or even turbulent separation. The ZZ tape is implemented on all BeRT blades at a chord-wise LE position of both the suction side (SuS) at $x_{SuS} = 5$ %c and the pressure side (PrS) at $x_{PrS} = 10$ %c. The BL thickness of the clean baseline, δ, is calculated with XFOIL (Drela, 1989) based on the Reynolds number, the AoA and the N-criterion (Ncrit) modeling the transition location. The design conditions are defined by $\alpha_{opt} \approx 5°$, $Re \approx 250k$ and Ncrit = 6 representing the relatively high Ti inside the test section. Depending on δ, the absolute height of the ZZ tape is adjusted in various steps to the chord-length, as depicted in Figure 4 (a).

2.2.2 Gurney Flaps

The GF-height is submerged by the BL thickness at the TE in order to keep the induced drag penalty on an acceptable level. XFOIL predicts the BL thickness at the TE to be $\delta_{TE} = 1.0$ %c, considering design conditions. In addition, another GF-height of half the local BL thickness is chosen, so that the GF configurations include $GF = 1$ %c and $GF = 0.5$ %c. Apart from the

very tip section, they are implemented in the form of thin angle profiles made of brass. One side of the angle profiles is cut in a linear way in order to match the linear chord decrease, as shown in Figure 4 (b). The other side of the profile is attached with thin double-sided adhesive tape immediately adjacent to the TE.

Figure 4. (a) Zig Zag tape at the leading edge of the suction side (b) Gurney Flaps and ZZ tape at the pressure side of the trailing edge

2.2.3 Test matrix

Table 1 summarizes the test matrix that consists of four blade configurations, three Operation Points (OPs) and three measurement methods. The OPs include the so-called stall, rated and feather conditions, which are characterized by low, rated and high TSR or AoA, respectively. Each test run has a total duration of 60 s. The Reynolds numbers are simulated with the Blade Element Momentum (BEM) simulation-module of QBlade (Marten et al., 2010).

Table 1. Test matrix

Blade configuration		
	Tripped case	Clean case
GF = 0.5%c	Operation points	
GF = 1.0%c		
Measurement method		
Ultrasonic Anemometry	Wake-velocities → AoA	
Pressure taps	c_p distribution → lift curve	
Strain gauges	Root bending moments	

Operation point (clean case)			
	Stall	**Rated**	**Feather**
TSR	3.0	4.3	5.6
AoA in °	16.5	8.6	4.6
Inflow velocity in ms⁻¹	6.5	6.5	5.0
Rot. Frequency in Hz	2.1	3.0	3.0
Re-number (mid-span)	200k	270k	260k

2.3 Measurement methods

The measurement methods shown in Table 1 consist of three types of sensors that are simultaneously recording the wake-velocity, the pressure distribution and the root bending moments.

135 ### 2.3.1 Ultrasonic Anemometry

3D Ultrasonic Anemometers (UAs) are widely spread in the wind energy industry. The technology is recognized by different wind industry standards such as the IEC 61400 to determine the power curve of wind turbines or the Association of German Engineers (VDI) for turbulence measurements. Also, there are numerous references for the use of UAs as part of wind tunnel campaigns, such as Weber (1995) and Cuerva (2003). The Anemometer is a commercial product of Thies CLIMA (version

140 4.383). According to the manufacturer, they are free from calibration and maintenance.
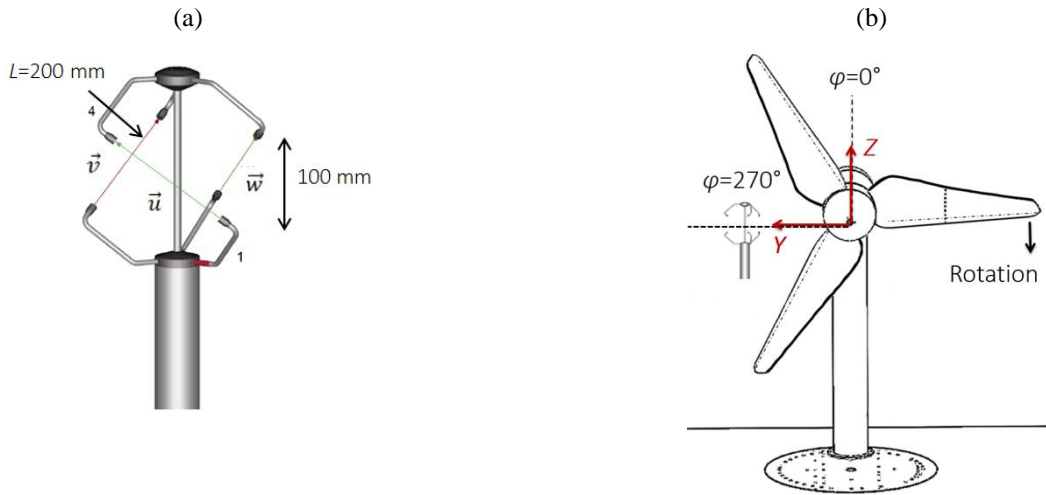
Figure 5. (a) Ultrasonic Anemometer 3D, reproduced and modified from Thies CLIMA. (b) Definition of the azimuthal blade positions looking downstream

Figure 5 (a) displays the three separate acoustic transmitter-receiver pairs that are installed orthogonally to each other. The velocity vectors, $\vec{u}$, $\vec{v}$ and $\vec{w}$, are determined by six individual measurements based on the bidirectional time-of-flight

145 principle, i.e. the duration of each signal to be sent and received,

$$\vec{u} = \frac{L}{2}\left(\frac{1}{t_1} - \frac{1}{t_2}\right),$$

(1)

where L = 200mm is the exact running-length between each sensor pair, so that the measurement volume amounts to (200 x 200 x 200) mm³. The velocity vectors $\vec{v}$ and $\vec{w}$ are calculated accordingly. Eq. (1) shows that the 3D velocity calculation

150 depends only on the average propagation velocity of the ultrasound, t_1 and t_2, which is delayed or accelerated, depending on the specific airflow. Hence, the output values are independent of the density and temperature of the air. Subsequently, the

velocity vectors are transformed to a natural coordinate system, so that the output time-series turns into the axial, lateral and vertical velocity components, u, v and w. The device-internal DAQ system consists of a half-duplex interface and is entirely independent of both the wind tunnel and the BeRT system. According to the manufacturer, the measurement accuracy is 0.1 ms⁻¹ per value. The data is recorded at a sampling rate of 60 Hz by means of LabVIEW tool developed by the authors.

Considering the relatively big measurement volume and the relatively low sampling rate, compared to e.g. hotwire or PIV-based devices, the UA is not adequate for the investigation of complex or high-speed flow structures. However, the BeRT wake-flow is expected to consist merely of an axial and a tangential velocity component due to the formation of a rotating wake tube. The impact of complex tip and root vortices on the wake is considered negligible in the mid-span blade region, as shown by Herráez et al. (2018).

The UA is installed at one static position, i.e. downstream ($X = 1.3R$), in the mid-span region ($Y = 0.56R$) and at hub height ($Z = 0R$), see Figure 5 (b). It is positioned vertically with a spirit level and turned around its own axis towards the axial inflow, so that the lateral and the vertical components, v and w, tend to zero. The set-up is fixed at its final position for all test-runs, which are presented in Sect. 3.

2.3.2 Pressure taps

The pressure distribution is extracted by means of 18 Pressure Taps (PTs) on the suction, and 12 on the pressure side located along the chord-length at $r = 0.45R$, see Figure 6 (a) and (b). Each orifice is connected via silicone tubing to its corresponding differential pressure sensor (HCL0025E), i.e. the pressure box inside the spinner. The experimental procedure and the data post-processing is based on Soto-Valle et al. (2019).
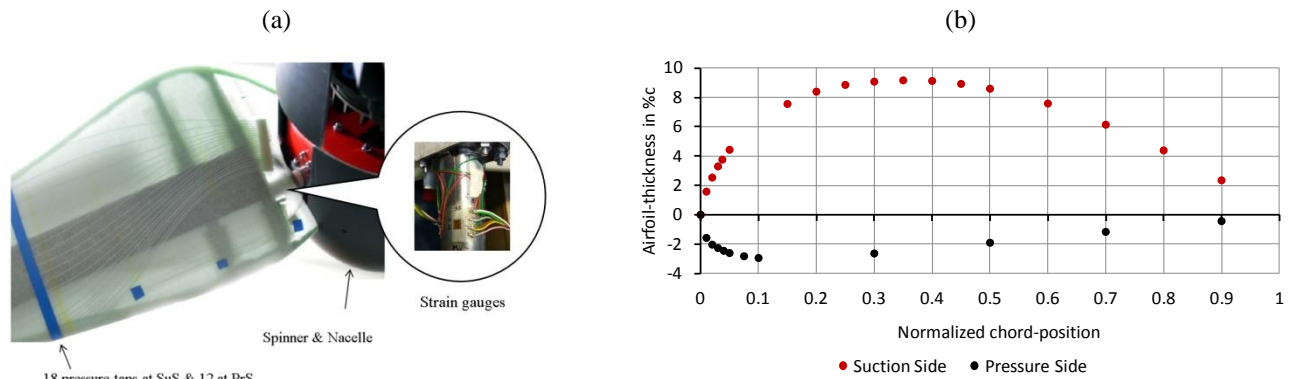
(a)   (b)

Figure 6. (a) BeRT blade and pressure taps, reproduced and modified from Fischer (2015). (b) Chord-wise position of pressure at $r = 0.45R$.

The differential pressure values are transformed into the pressure coefficient,

$$c_{p,PT} = \frac{\Delta p_{st,PT} + p_{rot}}{p_{dyn,ref}} = \frac{(p_{st,PT} - p_{st,\infty}) + (0.5\rho \cdot (\omega r)^2)}{p_{dyn,ref}},$$ (2)

where

- $\Delta p_{st,PT}$ is the difference between the absolute static pressure at each PT and the inflow Prandtl tubes $p_{st,\infty}$.
- p_{rot} refers to the additional pressure due to the rotation of the blade-element. It is added to $\Delta p_{st,PT}$ in the form of a constant correction term in accordance with Hand, et al. (2001).
- $p_{dyn,ref}$ describes the referential dynamic pressure, i.e. the effective flow velocity experienced by the blade element. According to Hand et al. (2001) it is determined by the maximum pressure that is recorded on the pressure side, the frontal stagnation point, where $c_{p,PT,ref} = 1$. According to Eq. (2) the referential dynamic pressure is determined by $p_{dyn,ref} = \Delta p_{st,PT,ref} + p_{rot}$.

The c_p values are phase-averaged over an azimuthal angle of $\varphi = 10°$, as shown in Figure 5 (b). Each PT provides a total of 36 pressure values at the following blade positions: $\varphi = [0°, 10°, 20° ... 350°]$, so that $\varphi = 270°$ contains the average of all data points between $265° < \varphi < 275°$.

Subsequently, Δc_p is calculated by subtracting the integrated c_p distribution of the PrS from the SuS. Next, the normal coefficient, c_n, and the tangential coefficient, c_t, are determined. Per definition, $\vec{c_n}$ is orthogonal to the chord-line pointing towards the SuS, while $\vec{c_t}$ is parallel to the chord-line pointing towards the LE. Following Hand et al. (2001),

$$c_n = \frac{1}{2} \cdot \sum_{i=1}^{30} \cdot \left(c_{p,PTi} + c_{p,PTi+1}\right) \cdot (x_{PTi+1} - x_{PTi}),$$ (3)

and

$$c_t = \frac{1}{2} \cdot \sum_{i=1}^{30} \cdot \left(c_{p,PTi} + c_{p,PTi+1}\right) \cdot (y_{PTi+1} - y_{PTi}),$$ (4)

where x and y are the normalized chord positions of each PT. The numbering starts at the TE ($x = 0.9$) with the 18 PTs on the SuS until the LE ($x = 0$) and proceeds with the 12 PTs on the PrS from the LE back to the TE. Finally, the lift coefficient is calculated in relation to the corresponding AoA, α, which are determined by the wake measurements of the UAS (Table 1).

$$c_l = c_n \cdot \cos(\alpha) + c_t \cdot \sin(\alpha).$$ (5)

The term $c_t \cdot \sin(\alpha)$ of Eq. (5) describes the pressure drag and is not containing the skin-friction drag, so that $c_t \cdot \sin(\alpha) < c_d$ (Barlow, 1999). Hence, for relatively small AoA, c_t is hardly influencing the c_l results, which are presented in Sect. 3.

2.3.3 Strain gauges

205 The strain gauges (SGs) are mounted at the clamping of the blade, see Figure 6(a). They are connected as a full-bridge configuration in order to mitigate temperature and cross talk effects. The experimental procedure to determine the Root Bending Moments (RBMs) is based on Bartholomay et al. (2018). For the purpose of the comparative investigation between baseline and GF configurations, a simplified post-processing protocol is applied that does not include the data-based cross talk correction.

210

Before testing each blade configuration, the offset signal is recorded in slow-motion at the lowest rotating frequency available, f_{rot} = 0.1 Hz. In this way, the gravitational RMBs, which are registered as a sinusoidal signal in the edgewise direction, is subtracted from the results. Moreover, at operational frequencies, the axial forces due to the blade rotation are causing a material deformation directed towards the blade tip. They are quantified as a combination of centrifugal and

215 gravitational forces by applying

$$F_{axial} = F_{cent} - F_{grav} = (m_{blade} \cdot r_{cg} \cdot \omega^2) - (m_{blade} \cdot g \cdot \cos(\varphi)), \tag{6}$$

where m_{blade} = 5.67 kg, the center of gravity is located at r_{cg} = 0.31R and φ refers to each phase-locked blade position. The rotational frequency is kept constant during each test-run, ω = const, so that the centrifugal force F_{cent} becomes a constant

220 correction term. The effective flapwise and edgewise RBMs, which are related to the aerodynamic loads acting on the blade, are then determined by the following equations.

$$M_{flap}(\varphi) = (U_{f,raw}(\varphi) - U_{f,off}(\varphi)) \cdot K_{f1} - (F_{axial} \cdot K_{f2}). \tag{7}$$

$$M_{edge}(\varphi) = (U_{e,raw}(\varphi) - U_{e,off}(\varphi)) \cdot K_{e1} - (F_{axial} \cdot K_{e2}). \tag{8}$$

225 Where

- M_{flap} and M_{edge} are the effective flapwise or edgewise RBMs in Nm due to the aerodynamic loads.
- $U_{f,raw}$ and $U_{e,raw}$ stand for the raw data signal in V.
- $U_{f,off}$ and $U_{e,off}$ describe the slow-motion offset signal in V.
- K_{f1} and K_{e1} refer to constant calibration factors to transform V into Nm.
230 - K_{f2} and K_{e2} refer to constant calibration factors to transform the axial forces from N into Nm

Applying Eq. (7) and (8) both the out-of-plane and the in-plane RBMs are computed for each of the 36 blade positions, as presented in Sect. 3.

3 Results

235 Unless stated otherwise, the results of the tripped case are presented in this section. The corresponding results of the clean case are accessible in Appendix A for completeness.

3.1 Wake velocities and angles-of-attack

Simultaneously to the inflow Prandtl tubes, the 3D wake velocities are recorded with the UA at one static position, i.e. at hub-height ($Z = 0R$ and $\varphi = 270°$), downstream ($X = 1.3R$) and in the mid-span blade area ($Y = 0.56R$), see Figure 5 (b).

(a)   (b)
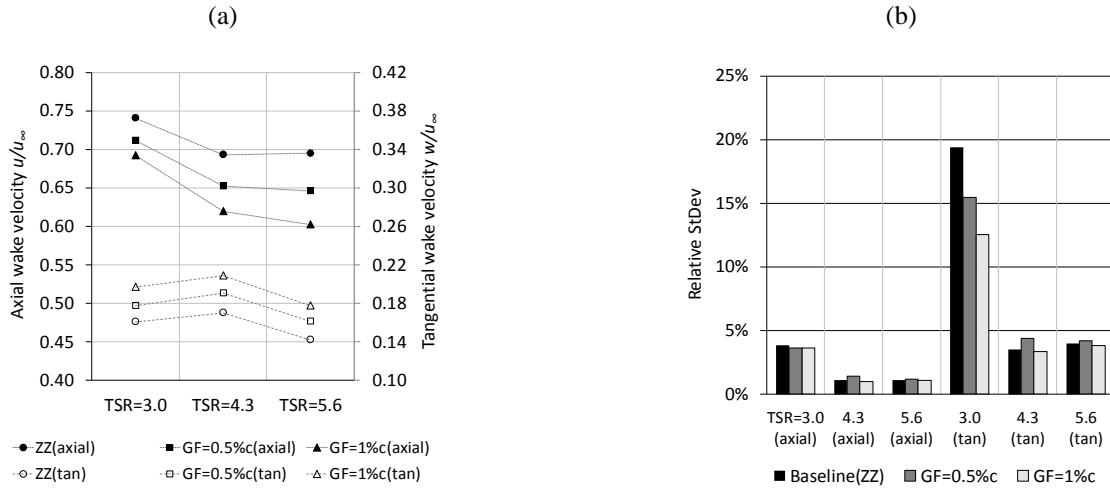
240 **Figure 7.** Tripped case. (a) Axial and tangential wake velocity. (b) Relative standard deviation of wake velocities.

Starting from the baseline case, the axial wake velocities shown in Figure 7 (a) are found significantly higher compared to typical free field conditions. According to the steady state BEM, the optimum axial wake velocity is supposed to be around one third of the inflow (Burton, 2011). In this case, it amounts to more than two thirds at rated conditions. This phenomenon is caused by the wind tunnel blockage effects, as shown via URANS simulations of the BeRT wake field using the fluid

245 dynamic code FLOWer. As such, Klein et al. (2018) predicts that the flow decelerates to an axial wake velocity of $0.62\, u_\infty < u_{CFD} < 0.77 u_\infty$, which is in agreement with the experimental results shown in Figure 7 (a), where $u_{EXP} = 0.69 u_\infty$.

Regarding the impact of GFs, Figure 7 (a) illustrates the consistent decrease of the axial, and the consistent increase of the tangential wake velocity, which is proportional to the GF-height. The lateral velocity component is neglected as it amounts

250 to $v << \pm 0.1$ ms^{-1}. The velocity standard deviation shown in Figure 7 (b) is normalized by the corresponding average velocity component and is therefore expressed in percentage. It primarily depends on the OP and is much higher when the blade is stalling, especially in terms of the tangential component. Hence, the initiation of flow separation is captured by the UA in the form of a more turbulent wake field. Overall, the GF configurations appear not to influence the wake turbulence

considerably, except for the tangential velocity component under stall conditions (*TSR* = 3.0), where the GFs appear to
mitigate the turbulence level.

The wake velocity is expressed by the axial and tangential rotor induction factors, *a* and *a'*, in order to determine the AoA at each blade-element. Following Burton (2011), they are defined by the following equations.

$$a = \frac{1}{2}\left(1 - \frac{u}{u_\infty}\right). \tag{9}$$

$$a' = \frac{w}{2\omega r}. \tag{10}$$

The induction factors describe the decrease of the axial, and the increase of the tangential velocity component from a reference point sufficiently far away from the rotor plane (Snel et al., 2009). In this case, the measurements are taken at a distance of $X = 1.3R$ downstream the rotor in order to avoid the influence of the wind tunnel contraction (Figure 3 (a)).

According to Hansen (2015) and Eq. (9) and (10), the AoA, α, is calculated for each blade element based on the following trigonometric operation:

$$\alpha = \arctan\left(\frac{(1-a)\ u_\infty}{(1+a')\ \omega r}\right) - \beta = \arctan\left(\frac{u_\infty + u}{2\omega r + w}\right) - \beta. \tag{11}$$

The twist-angle at the radial location of the pressure taps is $\beta(0.56R) \approx 9.8°$. The resulting AoA are given in Figure 8 (a).
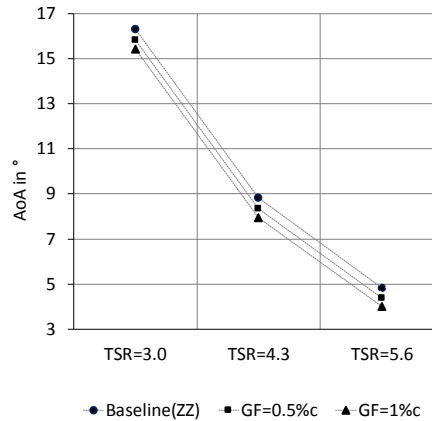

Figure 8. Angles-of-attack in the tripped case.

The consistent AoA-decrease caused by the GF configurations is displayed in Figure 8. Depending on the GF-height, it amounts to $\Delta\alpha_{GF=0.5\%c} = 0.5°$ and $\Delta\alpha_{GF=1.0\%c} = 0.9°$, in this case to a more favorable level. The results illustrate the basic impact of retrofitted GFs on the blade performance; decreasing axial wake velocities and thus AoA.

Furthermore, at rated conditions, the local AoA of the baseline case is found to be $\alpha = 8.8°$. This result is in general agreement with comparable investigations based on 3-hole probes (Bartholomay et al., 2017) and URANS simulations (Klein et al., 2018).

3.2 Pressure distribution and lift performance
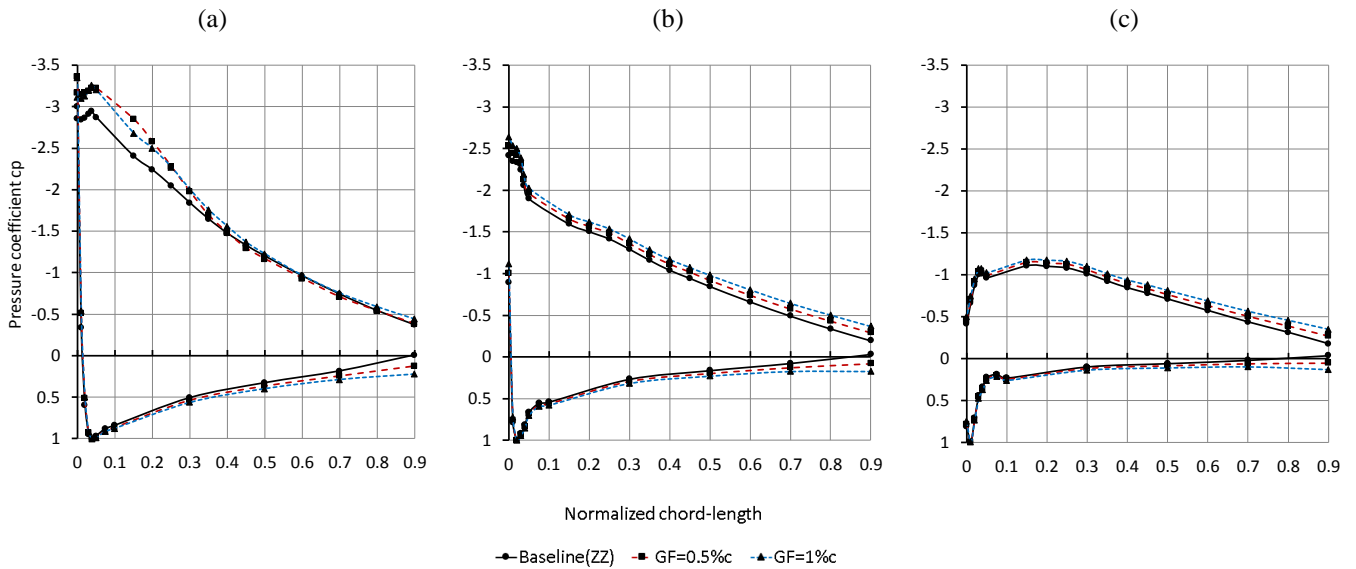
Figure 9. Pressure distribution in the tripped case at $\varphi = 270°$. (a) TSR = 3.0. (b) TSR = 4.3. (c) TSR = 5.6.

Figure 9 visualizes the c_p distribution at $r = 0.45R$ and considering the horizontal blade position, $\varphi = 270°$. Depending on the OP, Δc_p expands along the complete chord-length when applying GFs. This effect is particularly visible in terms of the aft-loading towards the TE. In fact, the aft-loading tail is one of the main design approaches of the DU airfoils in order to improve roughness sensitivity (Rooij and Timmer, 2003). At stall, $TSR = 3.0$, the separation at the SuS is not completed, despite the elevated AoA, $\alpha_{ZZ} = 16.3°$. Compared to XFOIL simulations, the maximum lift coefficient of the Clark-Y airfoil, $c_{l,max}$, is reached at approximately 14°. Hence, the stall delay seen in Figure 9 (a) is due to the radial flow due to the blade rotation.

In order to quantify the results the c_p distribution is transformed into the local lift curve based on Eq. (5). The required AoA are adopted from Sect. 3.1 (Figure 8), so that the lift coefficients combine the results of both the UA and the PTs.
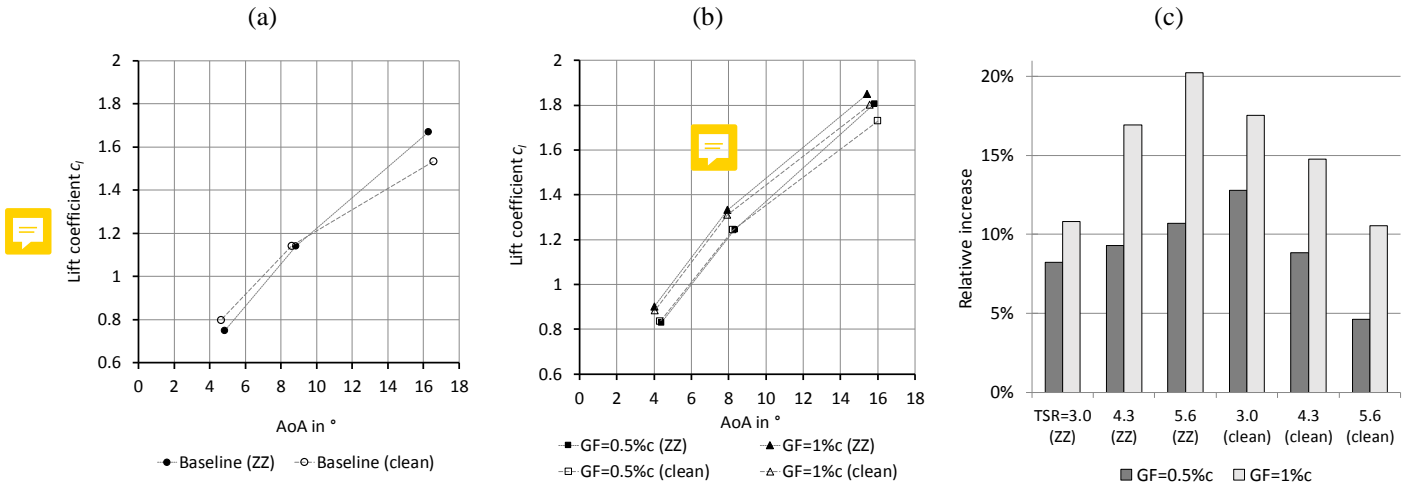
Figure 10. Lift coefficients over angles-of-attack in tripped and clean cases. (a) Baseline configurations. (b) Gurney flap configurations (c) Relative increase of Gurney flap configurations in relation to the corresponding baseline.

The lift coefficients are compared between the tripped and the clean cases, as depicted in Figure 10 (a). The tripped case results in smaller lift coefficients, $4° < \alpha < 5°$, due to the forced BL transition at the LE. However, at higher AoA, $8° < \alpha < 9°$, this is not the case anymore, while at stall, $15° < \alpha < 17°$, the ZZ tape appears to develop a beneficial effect on the lift performance. This phenomenon is probably caused by the tripped BL, which remains attached until closer to the TE. In the clean case, however, the less energetic boundary layer is separating earlier leading to smaller lift coefficients at higher AoA. ZZ tape leading to a smoother stall behavior is found by various wind tunnel experiments, such as Holst et al. (2016) based on the FX 63-137 airfoil at Re = 200k, using a 0.75 mm thick ZZ tape. Despite the decrease in the pre-stall, the lift coefficients prove to be on a similar level in the post-stall region.

In Figure 10 (b), the lift coefficients are compared between the tripped and the clean GF configurations. On the one hand, the benefit for the clean case is greater at stall, $15° < \alpha < 17°$, where the blade is underperforming compared to the tripped BL. On the other hand, the benefit for the tripped case is greater pre-stall, where the effect of the ZZ tape is more pronounced. This behaviour indicates that the GF configurations are alleviating the adverse effects of LE roughness. In fact, the lift performance in the tripped case is on a similar, or even higher, level for the complete AoA range, $4° < \alpha < 17°$.

The relative lift increase of both GF configurations in relation to the corresponding baseline cases is summarized in Figure 10 (c). At rated conditions, TSR = 4.3, the differences with respect to the tripped baseline amount to $\Delta c_{l,GF=0.5\%c}$ = 0.11 (9.3%) and $\Delta c_{l,GF=1.0\%c}$ = 0.19 (16.9%). Similar effects are also observed in the clean case.

In addition, the scale of Δc_l is in agreement with comparable wind tunnel experiment based on a Clark-Y airfoil section.

14
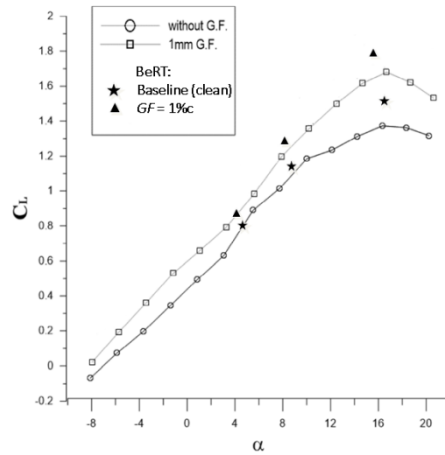
Figure 11. Lift coefficients of the Clark-Y airfoil including Gurney flap, reproduced and modified from Kheir-Aldeen (2014).

Figure 11 contrasts the lift coefficients of the clean Clark-Y airfoil section (th_{max} = 14%c, Re = 210k, GF = 1.2%c) and the clean Clark-Y blade element (th_{max} = 12%c, Re = 270k, GF = 1.0%c). The results demonstrate close similarities for both the baseline and the GF configurations. The slightly elevated lift values in case of the BeRT are probably due to the lower maximum thickness of the Clark-Y blade element. At $c_{l,max}$, the BeRT performance is characterized by the radial flow due to the blade rotation leading to stall delay. In case of the field rotor at the TU Delft, Rooij and Timmer (2003) report a shift of $c_{l,max}$ by several degrees towards higher AoA compared to numerical simulations of the identical 2D airfoil. After evaluating one area of the mid-span blade region, the following section investigates the impact of GFs on the SGs.
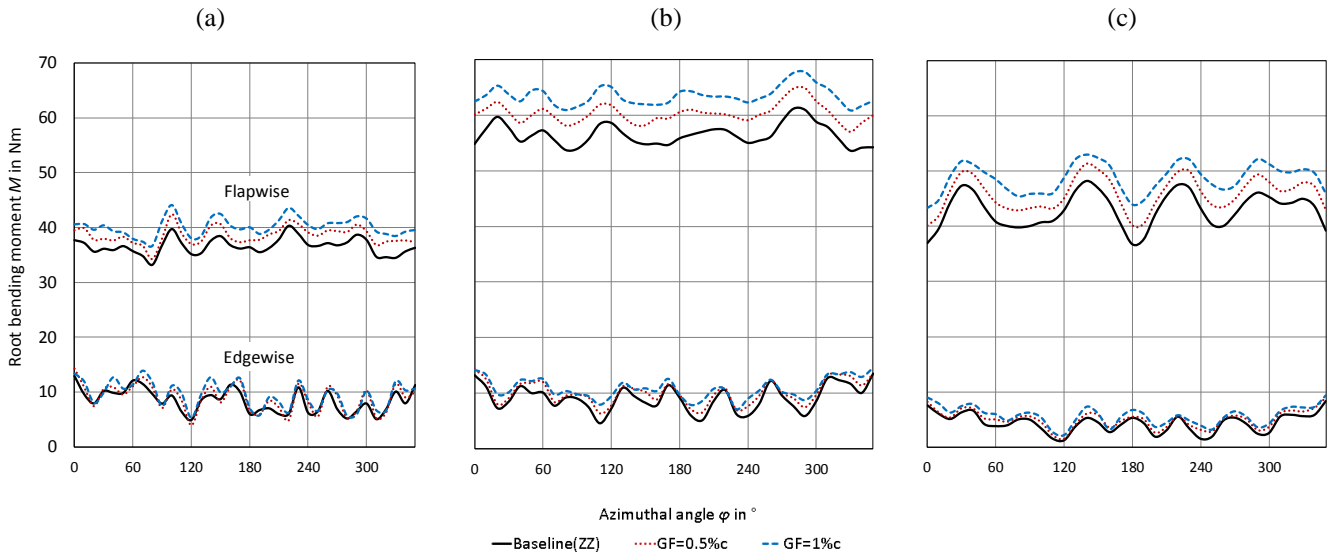
3.3 Root bending moments

Figure 12. Flapwise and edgewise root bending moments in the tripped case. (a) TSR = 3.0. (b) TSR = 4.3. (c) TSR = 5.6.

15

325 The integration of aerodynamic loads over the complete blade span yield the RBMs. The in-plane or edgewise RBMs are proportional to the rotor torque and thus the mechanical power output (Hansen, 2015). They are directly related to the out-of-plane or flapwise RBMs, which are proportional to the rotor thrust, i.e. the structural loads.

The effective RBMs due to the aerodynamic loads are calculated over one blade revolution, i.e. over all 36 phase-locked blade positions, as displayed in Figure 12. The impact of the GF configurations is registered as a consistent increase of both
330 the flapwise and the edgewise RBMs. The unsteady behavior of the curves is caused by the structural-dynamic excitation of the BeRT test bench, as previously observed by Bartholomay et al. (2017) and Bartholomay et al. (2018).

Next, the RBM curves are presented as average values of all 36 phase-locked blade positions in order to quantify and discuss
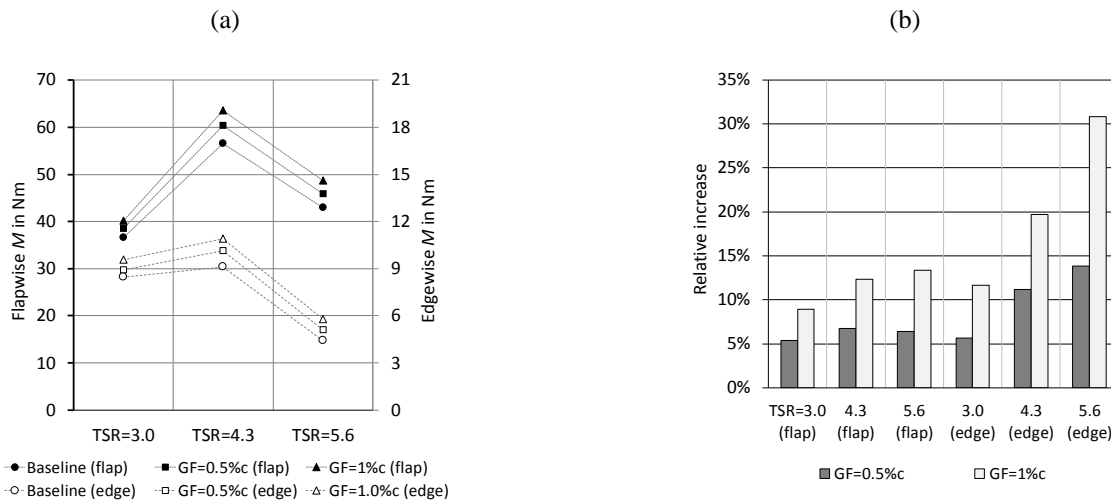335 the results.

(a)　　　　　　　　　　　　　　　　　　(b)

Figure 13. Tripped case. (a) Average flapwise and edgewise root bending moments (b) Relative increase to baseline

Figure 13 illustrates that, at rated conditions, the average increase of the flapwise RBMs amount to $\Delta M_{\text{flap,GF=0.5\%c}} = 3.8$ Nm (6.7%) and to $\Delta M_{\text{flap,GF=1.0\%c}} = 7.0$ Nm (12.4%). At the same time, the edgewise RBMs are enhanced by $\Delta M_{\text{edge,GF=0.5\%c}} = 1.0$ Nm (11.2%) and $\Delta M_{\text{edge,GF=1.0\%c}} = 1.8$ Nm (19.7 %). In the tripped case, the increase is more pronounced compared to the
340 clean case, especially towards higher TSR, i.e. smaller AoA.

This observation is in agreement with the relative changes of the local lift coefficients, previously shown in Figure 10 (c). In fact, the relative increase experienced by the lift performance appears to be related to the corresponding values of the edgewise RMBs. For instance, at rated conditions $\Delta c_{l,GF=0.5\%c} \approx 9.3\%$ versus $\Delta M_{\text{edge,GF=0.5\%c}} \approx 11.2\%$ and $\Delta c_{l,GF=1.0\%c} \approx 16.9\%$
345 versus $\Delta M_{\text{edge,GF=1.0\%c}} \approx 19.7$ %. Hence, both GF configurations evoke performance improvements in terms of the rotor torque, including the immanent augmentation of thrust.

16

4 Conclusions

The aerodynamic impact of Gurney flaps is investigated on the rotor blades of the Berlin Research Turbine of the Hermann-Föttinger Institute at the Technische Universität Berlin. The baseline measurements confirm the influence of the given wind tunnel blockage effects. At rated conditions and in the mid-span blade region, the axial wake velocity is approximately double in comparison to ideal free-field conditions. As such, the corresponding angles-of-attack are elevated in comparison to the design case and amount to $\alpha_{exp} = 8.8°$ rather than $\alpha_{opt} \approx 5°$.

In this situation, the retrofit applications of Gurney flaps lead to performance improvements in both the tripped and the clean cases. At rated conditions, the axial wake velocities are decreased and the angles-of-attack are reduced by $\Delta\alpha_{GF=0.5\%c} = 0.5°$ and $\Delta\alpha_{GF=1.0\%c} = 0.9°$. At the same time, the local lift coefficients are enhanced by $\Delta c_{l,GF=0.5\%c} = 0.11$ (9.3%) and $\Delta c_{l,GF=1.0\%c} = 0.19$ (16.9%), which is one of the main characteristic of Gurney flaps. Furthermore, the influence on the local lift performance is found more pronounced in the tripped case compared to the clean case. The effect of the aerodynamic loads over the complete blade span is analyzed in terms of the root bending moments. The average increase in the out-of-plane direction amounts to $\Delta M_{flap,GF=0.5\%c} = 3.8$ Nm (6.7%) and to $\Delta M_{flap,GF=1.0\%c} = 7.0$ Nm (12.4%). Simultaneously, the in-plane root bending moments are enhanced by $\Delta M_{edge,GF=0.5\%c} = 1.0$ Nm (11.2%) and $\Delta M_{edge,GF=1.0\%c} = 1.8$ Nm (19.7 %). Hence, decreasing angles-of-attack and increasing lift coefficients are accompanied by the enhancement of both the rotor thrust and the torque.

In summary, Gurney flaps are considered a worthwhile passive flow-control device for the use on horizontal axis wind turbines. The retrofit application is a useful option for the inner blade region in order to alleviate the effects of flow separation due to elevated angles-of-attack. Another promising effect of Gurney flaps is the reduced sensitivity to leading edge roughness throughout large parts of the blade span. However, the design of the Gurney flap-height is crucial in order to avoid adverse aerodynamic effects, such as induced drag and additional vortex shedding. Hence, further research is required quantifying the effect of different Gurney flap configurations on the dynamic loads and the overall energy yield of wind turbines.

Data availability. Measurement data and results can be provided by contacting the corresponding author.
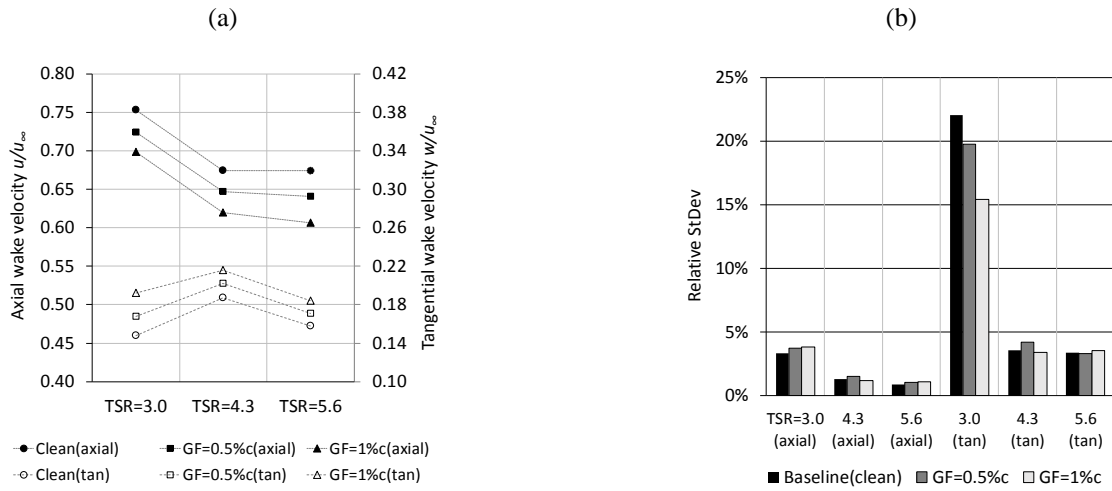
Appendix A: Results of the clean case

(a)

(b)

Figure A 1. Clean case. (a) Axial and tangential wake velocity. (b) Relative standard deviation of wake velocities.

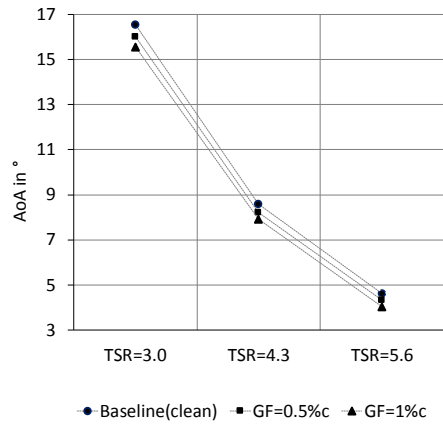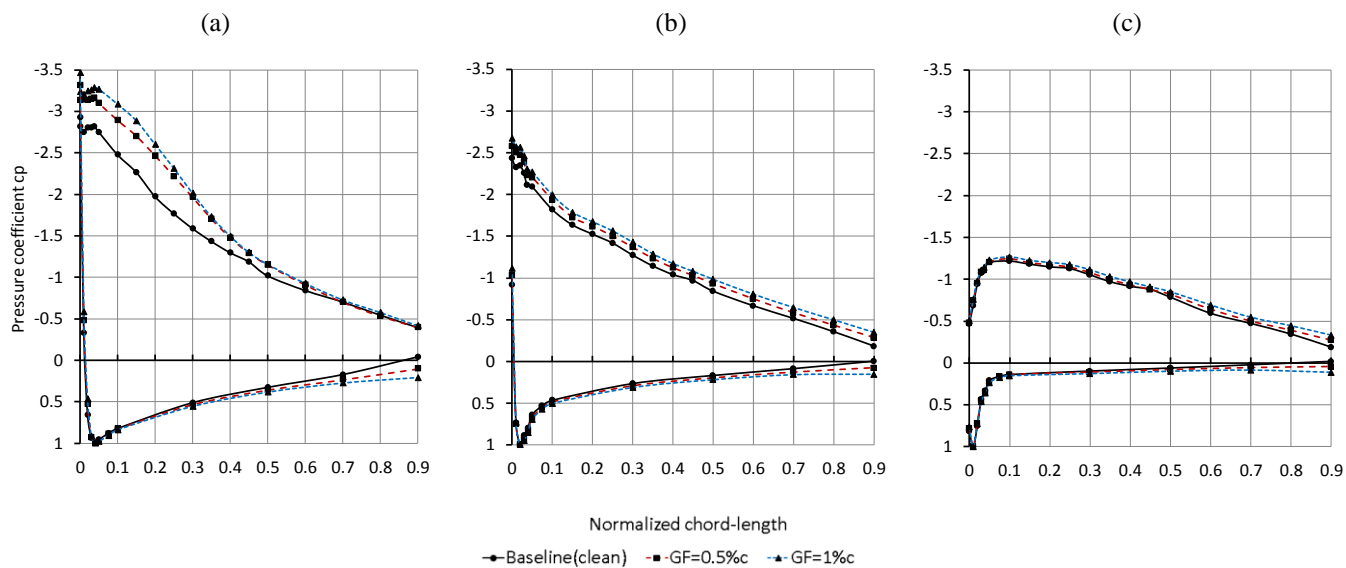**Figure A 2.** Angles-of-attack in the clean case.

(a)   (b)   (c)

380   **Figure A 3.** Pressure distribution in the clean case at $\varphi = 270°$. (a) TSR = 3.0. (b) TSR = 4.3. (c) TSR = 5.6.

(a)   (b)   (c)
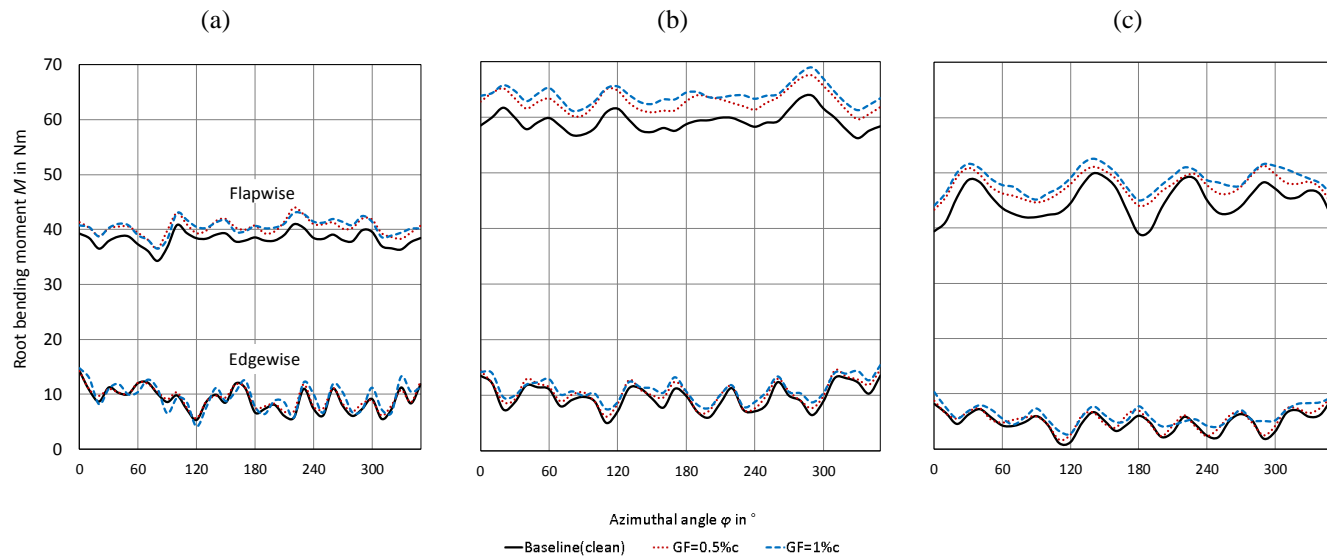
Figure A 4. Flapwise and edgewise root bending moments in the clean case. (a) TSR = 3.0. (b) TSR = 4.3. (c) TSR = 5.6.
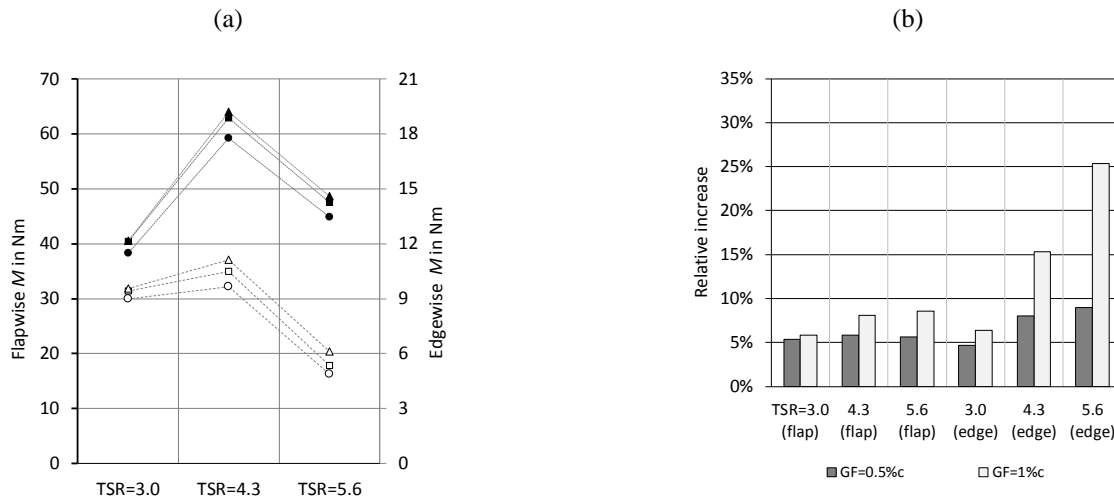
Figure A 5. Clean case. (a) Average flapwise and edgewise root bending moments (b) Relative increase to baseline

Author contribution

385 J. Alber performed the wind tunnel experiments together with R. Soto-Valle and the support of all co-authors. J. Alber processed the data and prepared the manuscript with the support of R. Soto-Valle, S. Bartholomay and M. Manolesos, all of whom contributed with important comments and suggestions to all section of the manuscript.

Competing interests

The authors declare that they have no conflict of interest.

References

395 Alber, J., Pechlivanoglou, G., Paschereit, C. O., Twele, J. and Weinzierl, G.: Parametric Investigation of Gurney Flaps, Proceedings of ASME Turbo Expo, 2017.

Bak, C., Zahle, F., Bitsche, R., Kim, T., Yde, A., Henriksen, L.C., Natarajan, A., and Hansen, M.: Description of the DTU 10 MW Reference Wind Turbine, Technical University of Denmark, DTU Wind Energy, 2013.

Barlow, J. B., Rae, w. h., Pope, A.: Low-Speed Wind Tunnel Testing, in: John Wiley & Sons, third edition, New York, USA,
400 1999.

Bartholomay, S., Fruck, W. L., Pechlivanoglou, G., Nayeri, C. N. and Paschereit, C. O.: Reproducible inflow modifications for a wind tunnel mounted research HAWT, Proceedings of the ASME Turbo Expo, 2017.

Bartholomay, S., Marten, D., Martínez, M. S., Alber, J., Pechlivanoglou, G., Nayeri, C. N., Paschereit, C. O., Klein, A. C., Lutz, T., and Krämer, E.: Cross-Talk Compensation for Blade Root Flap-and Edgewise Moments on an Experimental Research Wind Turbine and Comparison to Numerical Results, ASME Turbo Expo, 2018.

Bechert, D. W., Meyer, R. and Hage, W.: Drag Reduction of Airfoils with Miniflaps. Can we learn from Dragonflies?, AIAA Paper No. 2000-2315, 2000.

Burton, T., Jenkins, N., Sharpe, D. and Bossanyi, E.: Wind Energy Handbook, Second Edition, in: Wiley Interscience, United Kingdom, 2011.

Cuerva, A., Tejero, Sanz-Andrés, A. and Navarro, J.: On multiple-path sonic anemometer measurement theory, in: Exp. Fluids, Bd. 34, S. 345–357, 2003.

Drela, M.: XFOIL: An Analysis and Design System for Low Reynolds Number Airfoils, in: MIT: Massachusetts Institute of Technology, June 1989.

Fischer, J.:BWKA-1.5 TUB - Blades with Servo controlled Flaps, Technical Report, Smart Blade ®, Berlin, Germany, 2015.

Giguére, P., Lemayt, J. and Dumas, G.: Gurney flap effects and scaling for low-speed airfoils, AIAA Paper 1995-1881-CP, p.966-976, 1995.

Gruschwitz, E. and Schrenk, O.: A simple method for increasing the lift of airplane wings by means of flaps, Zeitschrift fuer Fluegtechnik und Motorluftschiffahrt, Vol 23 No 20, 1933.

Hand, M., Simms, D., Fingersh, L., Jager, D., Cotrell, J., Schreck, S. and Larwood, S.: Unsteady aerodynamics experiment phase VI: wind tunnel test configurations and available data campaigns, National Renewable Energy Lab, 2001.

Hansen, M. O. L.: Aerodynamics of Wind Turbines, in: 2nd Edition, Earthscan, United Kingdom, 2015.

Herráez, I., Daniele, E. and Schepers, J. G.: Extraction of the wake induction and angle of attack on rotating wind turbine blades from PIV and CFD results, in: Wind Energy Science, 3(1), 1–9, 2018.

Holst, D., Pechlivanoglou, G., Kohlrausch, C. T., Nayeri, C. N. and Paschereit, C. O.: SHAWT DESIGN: AIRFOIL AERODYNAMICS UNDER THE INFLUENCE OF ROUGHNESS, Proceedings of the ASME Turbo Expo, GT2016-56377, 2016.

Houghton, E. L.: Aerodynamics for Engineering Students, in: Aerodynamics for Engineering Students, 2013.

Kentfield, J.: The Influence of Free-Stream Turbulence Intensity on the Performance of Gurney-Flap Equipped Wind-Turbine Blades, Wind Engineering, 93-106, 1996.

Kheir-aldeen, D. M., and Hamid, A.: Experimental Study to the Effect of Gurney Flap on the Clark Y-14 Airfoil Wing Model, International Journal of Innovation and Scientific Research, 9(1), 120–132, 2014.

Klein, A. C., Bartholomay, S., Marten, D., Lutz, T., Pechlivanoglou, G., Nayeri, C. N., Paschereit, C. O., and Krämer, E. About the suitability of different numerical methods to reproduce model wind turbine measurements in a wind tunnel with a high blockage ratio, Wind Energy Science, 3(1), 439–460, 2018.

21

435   Liebeck, R. H.: Design of subsonic airfoils for high lift, in: Journal of Aircraft, 15(9), 547–561, 1978.

Marten, D. and Pechlivanoglou, G. (2010). Integration of a WT Blade Design tool in XFOIL/XFLR5. Proceedings of the DEWEK, 2010.

Pechlivanoglou, G., Fuehr, S., Nayeri, C. N. and Paschereit, C. O.: The Effect of Distributed Roughness on the Power Performance of Wind Turbines, Proceedings of the ASME Turbo Expo, GT2010-23258, pp. 845-855; 2010.

440   Pechlivanoglou, G., Philippidis T. P., Vey, S., Eisele, O., Nayeri, C. N. and Paschereit, C. O.: VORTEX GENERATORS FOR WIND TURBINE BLADES: WIND TUNNEL TESTS, FIELD SIMULATIONS AND STRUCTURAL ANALYSIS, Proceedings of the ASME Turbo Expo, RZGM2013-34, 2013.

Rooij, R P.J.O.M. van and Timmer, W. A.: ROUGHNESS SENSITIVITY CONSIDERATIONS FOR THICK ROTOR BLADE AIRFOILS, in: AIAA-2003-0350, 2003.

445   Schatz, M., Günther, B., and Thiele, F. Computational modeling of the unsteady wake behind Gurney-flaps, AIAA Flow Control Conference, 2004.

Snel, H., Schepers, J. G., and Siccama, N. B.: Mexico project: The database and results of data processing and interpretation, 47th AIAA Aerospace Sciences Meeting Including the New Horizons Forum and Aerospace Exposition, 2009.

Soto-Valle, R., Bartholomay, S., Alber, J., Manolesos, M., Nayeri, C. N., Paschereit, C. O.: Determining the Angle of
450   Attack along a Wind Turbine Rotor Blade in Wind Tunnel Experiments, Wind Energy Science, 2020.

Vey, S., Marten, D., Pechlivanoglou, G., Nayeri, C. and Paschereit, C. O.: Experimental and numerical investigations of a small research wind turbine, 33rd AIAA Applied Aerodynamics Conference, p. 3392, 2015.

Weber, F.I., Durgin, W. W. and Iohari, H.: Circulation Measurements About a Rapidly Pitching Airfoil Using An Ultrasonic System, AIAA 95-2269, 1995.

455   Wilcox, B. J., White, E. B. and Maniaci, D. C.: Roughness Sensitivity Comparisons of Wind Turbine Blade Sections, SANDIA REPORT, SAND2017-11288, 2017.

Zhang, Y., van Zuijlen, A. and van Bussel, G.: The MEXICO rotor aerodynamic loads prediction: ZigZag tape effects and laminar-turbulent transition modeling in CFD, Journal of Wind Engineering and Industrial Aerodynamics, 168(June), 152–163, 2017.